

# A 1-bit Time-Modulated Reflectarray for Reconfigurable-Intelligent-Surface Applications

Xianbo Cao<sup>1</sup>, Graduate Student Member, IEEE, Qiang Chen<sup>1</sup>, Senior Member, IEEE,  
Toru Tanaka, Masaki Kozai<sup>1</sup>, and Hiroya Minami

**Abstract**—The development of reconfigurable intelligent surfaces (RISs) is important to facilitate advances in beyond 5G and 6G technologies. However, the difficulty of controlling the reflected amplitude of the widely studied 1-bit reflectarray (RA) makes it difficult to meet the requirements of RIS for multiple application scenarios, and the change of the operating frequency in emerging time modulation (TM) technology-based RAs makes them unsuited to existing systems. Considering the observed the intrinsic similarities between the reflection states of 1-bit RA and logic states of 1-bit time function, a 1-bit time-modulated RA (1-bit TMRA) was designed based on a conventional 1-bit RA and TM technology in this study, and then was verified experimentally. The 1-bit RA characteristic was verified by realizing beam scanning, and the TM characteristic was verified by a shaping scattering pattern with ultralow sidelobe levels (SLLs). The results show that the proposed 1-bit TMRA is capable of realizing an extra TM characteristic without significantly increasing the system complexity of the 1-bit RA. Unlike most time-modulated arrays, the proposed 1-bit TMRA operates at the center frequency, making it suitable for direct application in existing wireless communication systems. These advantages highlight the potential of the proposed 1-bit TMRA for practical applications in RISs.

**Index Terms**—1-bit, reconfigurable intelligent surface (RIS), reflectarray (RA), time-modulated array (TMA).

## I. INTRODUCTION

**A**WARENESS of the pending resource depletion crisis has led to the proposal and vigorous development of renewable energy technologies. It is known that power fluctuations result in situations with no instant control and that distribution may result in energy waste and damage to the main power grid. Traditional centralized power and communication centers are vulnerable to severe damage in natural disasters. The development of container-type data centers that can be built flexibly is in response to the demand for more robust

Manuscript received 13 May 2022; revised 21 November 2022; accepted 29 November 2022. Date of publication 9 January 2023; date of current version 6 March 2023. This work was supported by the Program on Open Innovation Platform with Enterprises, Research Institute and Academia, Japan Science and Technology Agency (JST, OPERA) under Grant JPMJOP1852. (Corresponding author: Xianbo Cao.)

Xianbo Cao and Qiang Chen are with the Department of Communications Engineering, Tohoku University, Sendai 980-8579, Japan (e-mail: cao.xianbo.s7@dc.tohoku.ac.jp).

Toru Tanaka, Masaki Kozai, and Hiroya Minami are with the NTT Space Environment and Energy Laboratories, NTT Corporation, Tokyo 180-8585, Japan.

Color versions of one or more figures in this article are available at <https://doi.org/10.1109/TAP.2022.3233659>.

Digital Object Identifier 10.1109/TAP.2022.3233659

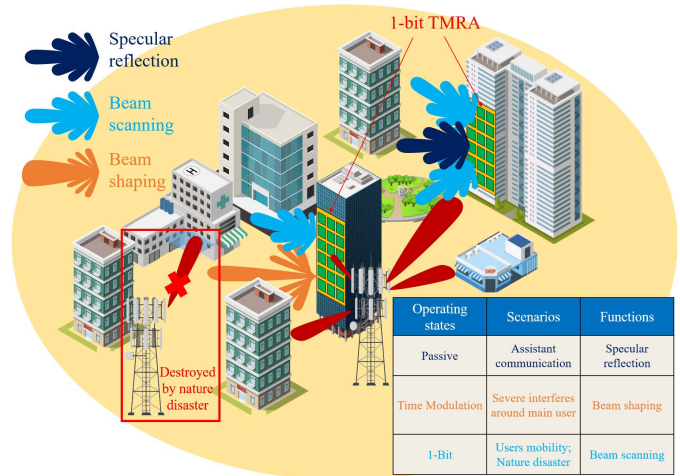


Fig. 1. Application scenarios of proposed 1-bit TMRA.

power and communication centers. Researchers have proposed the concept of resilient electric power and information communication technology (R-EICT) to achieve autonomous decentralized cooperative control of power and communications to improve energy efficiency and the disaster resilience of the power and communication system [1], [2]. The signal fading caused by electromagnetic scattering by buildings and other shielding has, however, made it challenging to connect container-type data centers to high-speed, broadband, and low-latency 5G/beyond 5G radio access networks (RANs). The reconfigurable intelligent surface (RIS) was introduced to address this issue.

The RIS, which has been attracting significant research attention, is defined as an intelligent surface integrated with electronically controlled elements that can flexibly modulate the reflective beam according to the requirements of the application scenario [3], [4], [5]. Among them, the real-time beam control achieved by the 1-bit reflectarray (RA) makes it suitable for RIS applications. The element of the 1-bit RA is connected to an electronically controlled device, and the state of the electronically controlled device can be controlled to obtain two reflection phases with a  $180^\circ$  (1-bit) difference. By selecting the 1-bit phase state of each element of the array to form a specific phase distribution, the direction of the reflected beam is controlled [6], [7], [8]. A Ku-band 1-bit RA element that achieves a 1-bit reflection phase using a p-i-n diode to connect the scattering patch to the ground was proposed by Yang et al. [10]. In this study, a 1-bit  $10 \times 10$  RA design based on the aforementioned 1-bit

element was experimentally verified to achieve beam scanning within a scan range of  $\pm 50^\circ$ . While the 1-bit RA allows flexibility in controlling the beam direction, it does not provide control of the reflected amplitude. As such, it does not meet the final requirement of beamforming for RIS applications.

Recently, time-modulated arrays (TMAs) are attracting attention because they allow the flexible control of both amplitude and phase distribution. The basic concept of TMAs is to modulate the array in a periodic manner by switching the RF switches ON and OFF to control the radiating status of the antenna elements in a predesigned time sequence [11]. The periodic switching of the array elements has the effect that the array antenna radiates signals at both the center frequency and harmonic frequencies. Importantly, an equivalent excitation (amplitude and phase) can be obtained in these harmonic frequencies, which can be controlled by the time sequence. Using harmonic components, TMA shows the powerful capacity of flexible beam control to realize such functions such as adaptive beamforming [12], interference nulling [13], beam steering [14], and direction of arrival (DoA) estimation [15], and multichannel communications [16].

The concept of time modulation (TM) has also been applied to RA. In 2014, the time-modulated RA (TMRA) was proposed by introducing TM into the design of RA. Wang and Tennant [17] proposed a 64-element TMRA, which uses a p-i-n diode as an RF switch and enables the TMRA element to achieve two states: a strongly reflective state and a non-reflective state. The high and low levels of the time sequence are realized by controlling the ON/OFF states of the diode. The use of a progressive timing sequence makes it possible to achieve reflected beams, which point in different directions at different harmonic frequencies. The scattering patterns for the first three harmonic frequencies have been experimentally verified in [17]. Lately, Dai et al. [18] proposed a space-time-coding metasurface, which operates at 24 GHz and can simultaneously realize beam control and direction finding with one set of time sequences, demonstrating the diversity of functions that can be achieved by TMRA. Among the large number of TMRA-based studies, which have recently emerged, various functions have been realized, including beamforming and scattering control [19], the realization of multimodulation schemes [20], spread-spectrum selective camouflaging [21], and stealth [22]. Although TMRA shows huge potential for RIS applications, at this point in time the flexible beam control is only realized in the harmonic frequencies. In other words, there is a change in the frequency of the totally controllable reflected beam (in terms of both amplitude and phase control). This is a challenge to the existing wireless communication system. The TMRA cannot be directly applied in the wireless communication system until the relevant issues are successfully resolved.

In this article, we first clarify the intrinsic similarities between the reflection states of 1-bit RA and the logic states of the 1-bit time function and then propose a novel 1-bit time-modulated RA (1-bit TMRA) for RIS applications. The control boards are designed, and the feed setup is optimized to obtain a complete 1-bit TMRA system. We then experimentally verify the proposed 1-bit TMRA using a  $10 \times 10$  prototype operating within the X-band. As shown in Fig. 1, the proposed 1-bit TMRA has the following features.

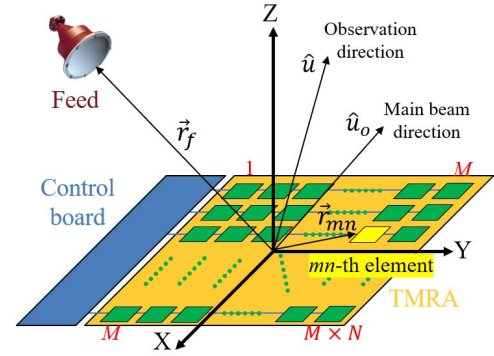


Fig. 2. Typical TMRA system.

- 1) The reflection direction is fixed in the main operating scenario. This is expected to provide a specular reflection of the reflected wave when the 1-bit TMRA works passively and also allow the control of the shape of the reflected wave when the 1-bit TMRA works in a TM state. The latter would make it possible to produce a reflected wave with ultralow sidelobe levels (SLLs).
- 2) The reflected beam can be pointed in any desired direction. It is expected that the 1-bit TMRA would work in a 1-bit RA state in specific operating scenarios, depending on the users' mobility or filling the coverage holes caused by damage to the original base station resulting from natural disasters.
- 3) The operating frequency of the incident carrier signal would not be changed for all operating states.

The rest of this article is organized as follows. Section II demonstrates the 1-bit TMRA concept. Section III describes the design and prototype of the TMRA element and system. In Section IV, specific validation experiments and a discussion of the measured results are presented. Finally, Section V concludes this work.

## II. 1-BIT TMRA CONCEPT AND DESCRIPTION

### A. Conventional TMRA Concept

As shown in Fig. 2, a typical TMRA system consists of a spatial feed source, an RA consisting of reflective elements connected to high-speed switches, and a TM control circuit. Unlike the RA, which requires adjustments of the reflected phase of each element to control the reflective characteristics of the array, the TMRA controls the reflective characteristics of the array by controlling the time-domain scattering characteristics generated by the ON/OFF switching of each element. Assuming a planar TMRA consisting of  $M \times N$  reflective elements, each reflective element is controlled by a switch to generate two reflective states: no reflection (denoted by "0") or strong reflection (denoted by "1"). As shown in Fig. 3(a), the switch is turned on and off periodically, and the corresponding turn on/off times are denoted as  $t_{\text{on}}$  and  $t_{\text{off}}$ , where  $kT_p \leq t_{\text{on}} \leq t_{\text{off}} \leq (k+1)T_p$  and  $T_p$  is the time of a complete switching cycle (denoted by a time-modulation period), and  $k$  is an integer. Under these conditions, the scattering waveform generated by the TMRA with the term  $e^{j2\pi f_c t}$  explicitly

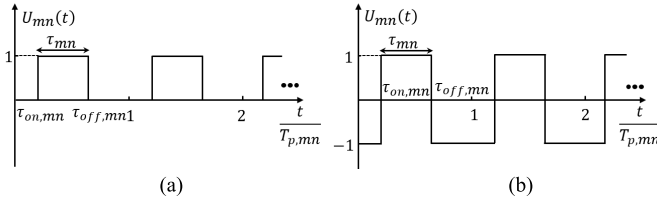


Fig. 3. TM function of the  $m$ th element. (a) Conventional time function. (b) Proposed 1-bit time function.

included is mathematically expressed as

$$f(t, \theta, \varphi) = e^{j2\pi f_c t} \sum_{m=1}^M \sum_{n=1}^N E_{mn}(\theta, \varphi) U_{mn}(t) \quad (1)$$

where  $f_c$  and  $k_c$  are the frequency and the free-space wavenumber, respectively, of the illuminating continuous wave signal,  $E_{mn}(\theta, \varphi)$  is the static scattering pattern of the  $m$ th element, which is described as [23]

$$E_{mn}(\theta, \varphi) = (\cos\theta)^{q_e} \frac{[\cos\theta_f(mn)]^{q_f}}{|\vec{r}_{mn} - \vec{r}_f|} e^{-jk_c(|\vec{r}_{mn} - \vec{r}_f| - \vec{r}_{mn} \cdot \hat{u})} \times [\cos\theta_e(mn)]^{q_e} e^{j\varphi_{mn}} \quad (2)$$

where  $q_f$  and  $q_e$  are the pattern function values of the feed and RA element, respectively.

In (1),  $U_{mn}(t)$  is the TM function to control the switch ON/OFF of the  $m$ th element, which can be described by

$$U_{mn}(t) = \sum_{k=-\infty}^{\infty} g_{mn}(t - kT_{p,mn}) \quad (3)$$

where  $T_{p,mn}$  is the TM period of the  $m$ th element and  $g_{mn}(t)$  is the TM function of the  $m$ th element. This is expressed by the following:

$$g_{mn}(t) = \begin{cases} 1, & t_{\text{on},mn} \leq t \leq t_{\text{off},mn} \\ 0, & \text{elsewhere.} \end{cases} \quad (4)$$

Correspondingly, the TMRA is reflective when the TM function is “1” and is nonreflective when the TM function is “0.” According to the Fourier series theory,  $U_{mn}(t)$  can be written in the sum of an infinite number of harmonic frequency components, as

$$U_{mn}(t) = \sum_{h=-\infty}^{\infty} a_{n,mn} e^{j2\pi h f_{p,mn} t} \quad (5)$$

where  $h$  is an integer representing the number of harmonic frequency components. The modulation frequency  $f_{p,mn}$  is defined as the inverse of the modulation period. The Fourier series coefficients  $a_{mn,h}$  of the  $m$ th element can be expressed as

$$a_{mn,h} = \frac{1}{T_{p,mn}} \int_{t_{\text{on},mn}}^{t_{\text{off},mn}} g_{mn}(t) e^{-j2\pi h f_{p,mn} t} dt = \begin{cases} \tau_{mn} \text{sinc}(\pi h \tau_{mn}) e^{-j\pi h (\tau_{\text{off},mn} + \tau_{\text{on},mn})}, & h \neq 0 \\ \tau_{mn}, & h = 0 \end{cases} \quad (6)$$

where  $\text{sinc}(\cdot)$  is the sampling function, which is defined by  $\text{sinc}(x) = \sin(x)/x$ . The  $\tau_{\text{on},mn}$  and  $\tau_{\text{off},mn}$  are the normalized turn on/off times of the  $m$ th element and are defined

by  $\tau_{\text{on},mn} = t_{\text{on},mn}/T_{p,mn}$  and  $\tau_{\text{off},mn} = t_{\text{off},mn}/T_{p,mn}$ . The  $\tau_{mn}$  is the switch-on duration and is defined by  $\tau_{mn} = \tau_{\text{off},mn} - \tau_{\text{on},mn}$ .

Therefore, the whole scattering pattern of TMRA in the frequency domain can be written as

$$f(\theta, \varphi) = \sum_{h=-\infty}^{\infty} \sum_{m=1}^M \sum_{n=1}^N E_{mn}(\theta, \varphi) a_{mn,h} = \sum_{h=-\infty}^{\infty} \sum_{m=1}^M \sum_{n=1}^N (A_{s,mn} A_{t,mn}^h) e^{j(\varphi_{s,mn} + \varphi_{t,mn}^h)} \quad (7)$$

where  $A_{s,mn}$  and  $\varphi_{s,mn}$  are the amplitude and the phase of  $E_{mn}(\theta, \varphi)$ , defined as the static amplitude and phase distribution. The  $A_{t,mn}^h$  and  $\varphi_{t,mn}^h$  are the amplitude and the phase of  $a_{mn,h}$ , defined as the time-modulated equivalent amplitude and phase distribution of the  $h$ -th harmonic frequency component.

The scattering characteristics of the TMRA can be manipulated by controlling  $\tau_{\text{on},mn}$  and  $\tau_{\text{off},mn}$ . This allows beam-forming at arbitrary harmonic frequencies to be realized. The  $\tau_{\text{on},mn}$  and  $\tau_{\text{off},mn}$  can be directly calculated from the desired aperture amplitude and phase distribution by (6). Note that the static amplitude and phase distribution are compensated by the time-modulated equivalent amplitude and phase distribution, thereby alleviating the limitation on the fabrication size of the TMRA element and improving the design flexibility.

### B. 1-bit TMRA Concept

While the conventional TMRA can realize beam-forming, it has been reported that TMRA can only control beam direction at harmonic frequencies ( $f_c + hf_p, h = \pm 1, 2, \dots$ ) (6). That is, the operating frequency changes when beam steering is performed. Additional filtering and frequency conversion circuits are required in practical applications. These inevitably increase the complexity and cost of the system and also pose a challenge to the framework of existing wireless communication systems.

By replacing the conventional time function with the 1-bit time function and corresponding it with the reflection states of 1-bit RA, the proposed 1-bit TMRA can achieve the following.

- 1) Compatibility with existing 1-bit RA systems, i.e., with the characteristics of beam scanning of 1-bit RA at the operating frequency.
- 2) Equivalent amplitude weighting at the operating frequency to obtain control of the beam shape with almost no increase in the complexity of the 1-bit RA system.

As can be seen from Fig. 3(b), the 1-bit time function has two states, “1” and “−1,” which correspond to the two states  $Ae^{j\varphi}$  and  $Ae^{j(\varphi+\pi)}$  in the 1-bit RA design. This correspondence naturally establishes an intrinsic connection between the 1-bit time function and the 1-bit RA, which not only makes it possible to design a 1-bit TMRA but also does not increase the complexity of the system except requiring the necessary TM control circuit to be added. Since the proposed 1-bit TMRA is designed to operate only at the center frequency ( $f_c$ ), it can be directly integrated with existing wireless communication systems. It is important to note that, strictly speaking, any two independent states can be described as 1-bit. In this case, we use 1-bit to specifically refer to two states with the same

amplitude but which are  $180^\circ$  out of phase. The Fourier series at the center frequency can be expressed as

$$a_{mn} = 2\tau_{mn} - 1. \quad (8)$$

It can be easily found that the TM can achieve any amplitude distribution required for the radiation pattern synthesis problem, including the Chebyshev distribution, Taylor distribution, and binomial distribution. The combination of 1-bit and TM provides one additional degree of freedom that can be used to improve some antenna performances, such as the reduction of SLLs and better beam shaping capability. Here, we give an arithmetic example to illustrate how a 1-bit TMRA shapes the reflected beam with the Chebyshev distribution at the center frequency. It is assumed that there is a 1-bit  $10 \times 10$  TMRA with an element spacing of half wavelength of the center frequency. The element is set as omnidirectional for simplicity, and a plane wave is obliquely incident on the surface of the 1-bit TMRA with an incidence angle of  $(\theta_{inc}, \varphi_{inc}) = (-30^\circ, -15^\circ)$ . The goal of the TM is to reduce the SLLs of the reflected beam and to shape the reflected beam with equal SLLs of  $-30$  dB (a Chebyshev pattern synthesis). Note that the Taylor distribution and the binomial distribution can also be realized by this method. The details of the procedures are demonstrated as follows. First, the desired normalized amplitude distribution of the 1-bit TMRA for realizing equal SLLs of  $-30$  dB is calculated from the Chebyshev polynomials [24]. This desired amplitude distribution is the time-modulated equivalent amplitude distribution  $a_{mn}$ , as shown in Fig. 4(a). Second, using (8), the corresponding normalized switch-on duration distribution  $\tau_{mn}$  is obtained from equivalent amplitude distribution, as shown in Fig. 4(b). Finally, by adopting the corresponding time signal to each element, the theoretical scattering pattern is calculated, as shown in Fig. 4(c). It can be clearly observed that the reflected beam has equal SLLs of  $-30$  dB and toward to  $(30^\circ, 15^\circ)$  direction. Because only the amplitude is modulated in this application, the reflected direction does not change.

More importantly, it can be seen from Fig. 4(a) and (b) that the dynamic range of the required time series is much smaller than the dynamic range of the original desired current distribution. This advantage allows the TM to achieve a large dynamic range and “current jumping” Chebyshev current distribution, which is difficult to accomplish with conventional amplitude-controllable RAs [25].

### C. Errors Analyses of 1-bit TMRA Realization

As mentioned, at the core of the proposed 1-bit TMRA concept is the similarity between the two reflected states and the two logic states of the time function. As such, it is necessary to analyze the influence on the TM when the reflected states deviate from their theoretical states. Assuming the time-modulated equivalent excitations of the “1” and “-1” states are  $E_1$  and  $E_{-1}$ , respectively, we obtain the following:

$$E_1 = A_1 e^{j\varphi_1} \text{ and } E_{-1} = A_{-1} e^{j\varphi_{-1}} \quad (9)$$

where  $A$  and  $\varphi$  are the equivalent amplitude and phase. Theoretically, the relationships should be as follows:

$$A_{-1} = A_1, \quad \varphi_{-1} - \varphi_1 = 180^\circ. \quad (10)$$

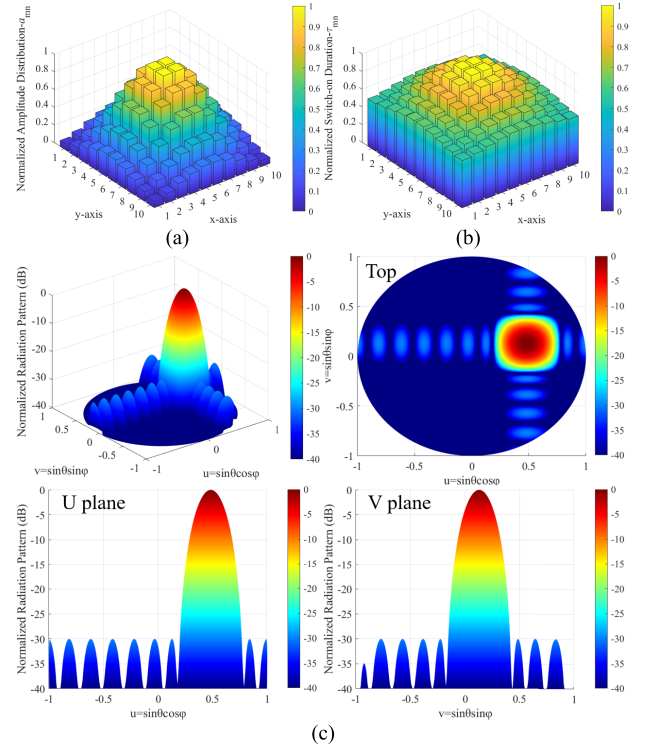


Fig. 4. Arithmetic example of 1-bit TMRA concept for realizing scattered pattern with equal SLLs of  $-30$  dB. (a) Desired amplitude distribution. (b) Corresponding switch-on duration distribution. (c) Theoretical scattering pattern.

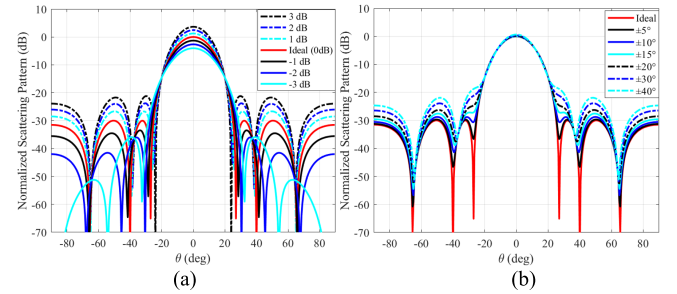


Fig. 5. Influence of errors of the amplitude and phase on TM. (a) Amplitude error. (b) Phase error.

The corresponding relationships should, however, be revised as follows to reflect the discrepancies expected in actual applications:

$$A_{-1} = A_1 e^{-\frac{\Delta A}{20}}, \quad \varphi_{-1} - \varphi_1 = 180^\circ + \Delta \varphi \quad (11)$$

where  $\Delta A$  and  $\Delta \varphi$  are amplitude error (dB) and phase error (degree), respectively.

The target of TM is to shape the reflected beam with equal SLLs of  $-30$  dB. For simplicity, the vertical incidence is considered. The calculated results, all normalized to the ideal result, are plotted in Fig. 5. It can be observed from Fig. 5(a) that when  $\Delta A$  is larger than 0, as  $\Delta A$  increases, both the main beam and sidelobes increase simultaneously, and the overall SLLs increase as well; however, when  $\Delta A$  is less than 0, as  $\Delta A$  decreases, the SLLs are no longer equal although the max SLL decreases, and the difference increases as  $\Delta A$  decreases. It can be found that when  $\Delta A = -3$  dB, the

shape of the scattering pattern and the SLLs do not meet the design requirements at all. These results suggest that in the 1-bit TMRA design,  $-3 \text{ dB} < \Delta A \leq 0 \text{ dB}$  should be satisfied to ensure the expected results are obtained.

On the other hand, it can be seen from Fig. 5(b) that the SLLs overall as  $\Delta\varphi$  increases, and the first sidelobe gradually deteriorates and overlaps with the main beam when  $\Delta\varphi$  is greater than  $\pm 20^\circ$ . For this reason, the 1-bit TMRA should be designed and implemented in such a way that the phase difference between the two reflective states is kept within the operating band of  $180^\circ \pm 20^\circ$ . It should be pointed out that the error analyses are based on the realization of equal SLLs of  $-30 \text{ dB}$ . While the specific threshold value may differ in other TM applications, the analysis method described here is universal.

### III. DESIGN AND PROTOTYPE

#### A. 1-bit TMRA Element

The configuration of the proposed 1-bit TMRA element is shown in Fig. 6(a) and (b). The tunable resonator approach [26] is adopted to control the reflection. The polarization of the electric field is along the  $x$ -axis. The microstrip patch as a scatterer is printed on the top side of the element and connected to one end of the phase delay line printed on the bottom side through the metallization vias. A p-i-n diode is placed in the middle of the phase delay line, and the resonant property of the element is changed by biasing the circuit to turn the diode ON or OFF the diode, thus obtaining a  $180^\circ$  phase difference. The bias point is positioned at the zero-electric-field point at the center of the microstrip patch. Moreover, an open-ended radial stub and a quarter-wavelength microstrip line are designed to choke the RF signal. These approaches ensure good isolation of dc and RF performance and reduce the additional loss resulting from the bias network. In this design, the phase delay line, bias circuit, p-i-n diode, and the associated solders are arranged such that they are placed on the bottom side below the ground to avoid undesired scattering and the deterioration of the radiation performance of the 1-bit TMRA.

The initial structure of the element is inspired by the work reported by Yang et al. [10]. To achieve a center operating frequency of 10 GHz, the periodicity of the element  $p$  is set at 10 mm ( $1/3\lambda_0$ ,  $\lambda_0$  is the free-space wavelength at 10 GHz) to avoid grating lobes. The main geometrical parameters of the 1-bit TMRA element are as follows:  $l_x = 7 \text{ mm}$  and  $l_y = 6 \text{ mm}$ . The thicknesses of the three substrate layers from top to bottom are 1.5, 0.1, and 0.5 mm, respectively. Since it offers low insertion loss and ultrahigh switching speed, MACOM MA4AGFCP910 is chosen as the p-i-n diode, which acts as a switch in TM. As shown in Fig. 6(b) for ON or OFF state, the p-i-n diode is modeled as a series of lumped resistance ( $R$ ) and inductance ( $L$ ) or capacitance ( $C$ ) and inductance ( $L$ ), respectively [27]. Fig. 6(c) shows the simulated reflection amplitude and phase difference under vertical incidence using Floquet ports and periodic boundaries in HFSS. At 10 GHz, the  $180^\circ$  phase difference is obtained when the p-i-n diode turns from one state to another. From 9.72 to 11.03 GHz, the phase difference between the two states is within  $180^\circ \pm 20^\circ$ , indicating good element-bandwidth

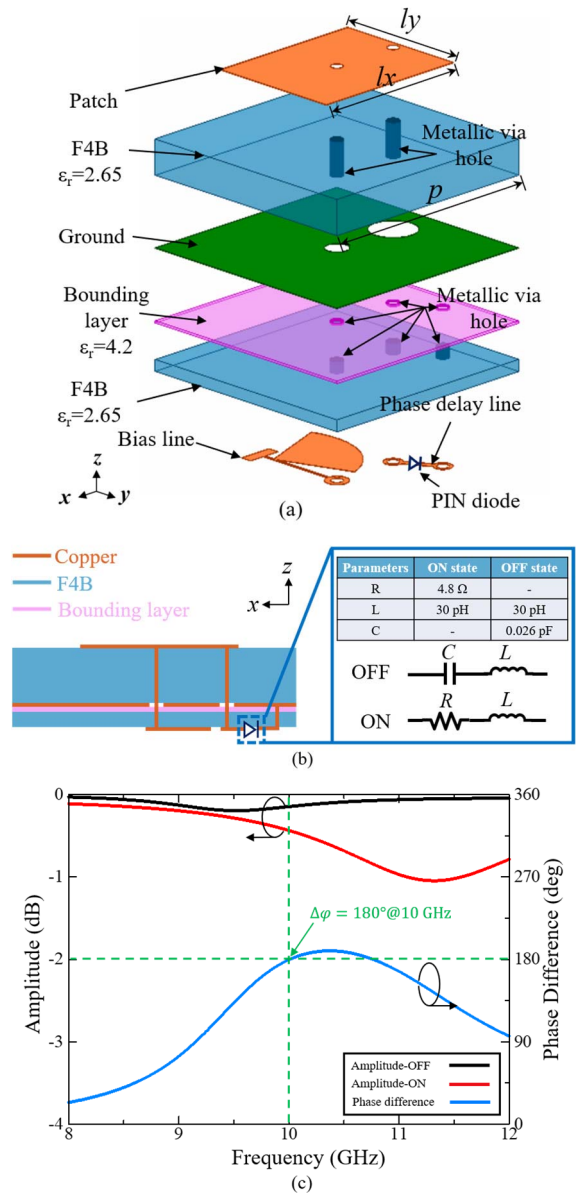


Fig. 6. 1-bit TMRA element. (a) Perspective view. (b) Side view and diode modeling. (c) Simulated reflection amplitude and phase difference for the two states.

performance. The element loss is less than  $-1 \text{ dB}$  within the frequency band of interest, regardless of the p-i-n states.

For experimental validation, the  $1 \times 2$  1-bit TMRA elements are fabricated and measured using the waveguide simulator [28]. Although the waveguide simulator can only evaluate the reflection characteristics of the prototype element at a certain oblique incident angle in the TE mode, which is different from the vertical incidence case of TEM mode in the simulation of element design, this method offers a rapid and low-cost method for verifying the design process and is widely used in the research of the large-scale reconfigurable RA [29], [30], [31]. The front and back views of the fabricated prototype element are shown in Fig. 7(a). Wires are soldered with the element to offer dc power for biasing the diodes. Fig. 7(b) shows the photograph of the waveguide assembled with the fabricated prototype element. The model of the waveguide is

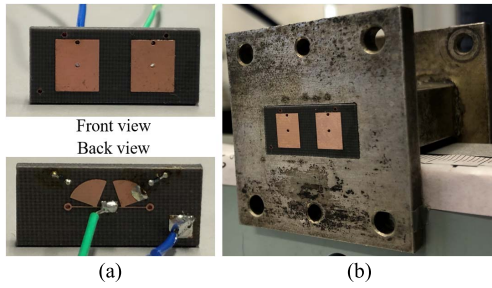


Fig. 7. Photographs of fabricated element prototype and assembly with a waveguide. (a)  $1 \times 2$  1-bit TMRA element prototype. (b) Assembly with a waveguide.

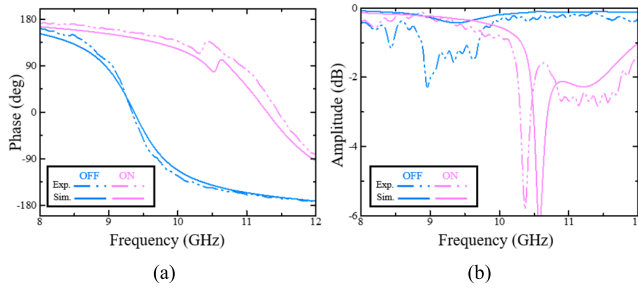


Fig. 8. Comparison between simulated and measured reflection coefficients. (a) Reflection phases. (b) Reflection amplitudes.

WR90 with a cross section of  $22.86 \times 10.16$  mm, which is just enough to accommodate the prototype element. In the experiment, the prototype element is located at the surface of the waveguide, and the assembled waveguide is connected to a coaxial-to-WR90 transition structure. The other side of the transition structure is connected to the vector network analyzer (VNA) with the model of Anritsu MS46122B-020. Therefore, the reflection coefficient at the surface of the prototype element can be directly measured after using TRL calibration on the transition structure.

For comparison purposes, a WR-90 waveguide model is built, and the  $1 \times 2$  1-bit TMRA elements are placed in it for simulation. Fig. 8 shows the simulated and measured reflection coefficients. It can be seen from Fig. 8(a) that the simulated and measured reflection phases are in good agreement. As shown in Fig. 8(b), despite the small differences in the reflection amplitude of the OFF state, they are all above  $-1$  dB near 10 GHz. In addition, the resonance at the ON state is caused by the oblique incidence in the waveguide, which is not characteristic of the element itself. These slight differences can be attributed to the fabrication tolerance and assembly misalignment among the waveguide, the transition structure, and the fabricated sample. Therefore, 1-bit phase reconfigurability with low loss is achieved, making it suitable for large 1-bit TMRA designs.

### B. 1-bit $10 \times 10$ TMRA Prototype

Based on the proposed element structure, we designed and fabricated a 1-bit TMRA prototype using printed circuit board (PCB) technology, as shown in Fig. 9. The 1-bit TMRA has an aperture of  $100 \times 100$  mm ( $3.33\lambda_0 \times 3.33\lambda_0$ ). Each element is soldered with a p-i-n diode and connected to a specific bias line to achieve 100 elements that are independently

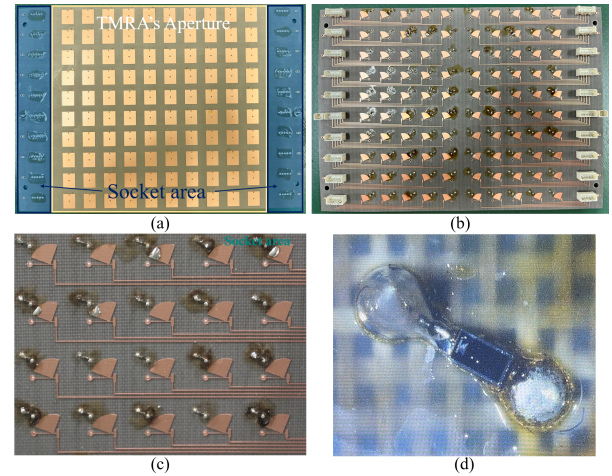


Fig. 9. 1-bit  $10 \times 10$  TMRA prototype. (a) Top view. (b) Bottom view. (c) Detail of the bias lines. (d) Detail of p-i-n diode soldering.

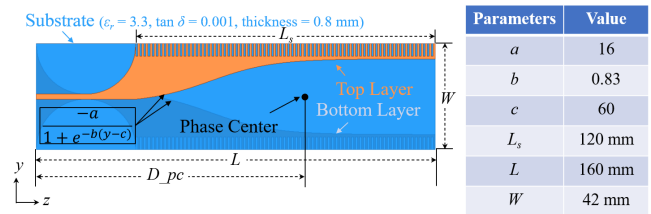


Fig. 10. APFA schematic view.

controllable. The TMRA and the control board are soldered with sockets, which are connected to each other by flat cables. Since each socket controls five elements independently, so there are 20 sockets soldered to the TMRA, symmetrically arranged on both sides of the TRMA. Through the control board, 100 elements can be independently controlled to realize 1-bit and TM characteristics.

### C. Feed Source Selection and System Design

The near-field feed method is widely used in reconfigurable RA systems to realize higher aperture efficiency [10]. Although the corrugated horn antenna, which provides a symmetric radiation pattern and excellent antenna efficiency, is widely used in RA design. Its bulk would cause severe blockage for such a small aperture of the fabricated 1-bit TMRA prototype. Instead, in this work, a printed antipodal fermi antenna (APFA) with tapered slots [32] is used as the feed source with the advantages of small volume, low profile, and lightweight, where the schema and the parameters are shown in Fig. 10. The APFA is linear polarization with the polarized direction along the short side. Two opposite slots are etched on both sides of the dielectric substrate, with the slot curve satisfying the Fermi–Dirac function. The operating principle and detailed characteristics of the APFA can be found in [32] and are omitted in this article. Therefore, only the radiation characteristics of interest are shown here and plotted in Fig. 11. All the results are obtained by the full-wave simulation via high-frequency structure simulator (HFSS). The realized gain and radiation efficiency are shown in Fig. 11(a), indicating the high gain and high efficiency of the APFA.

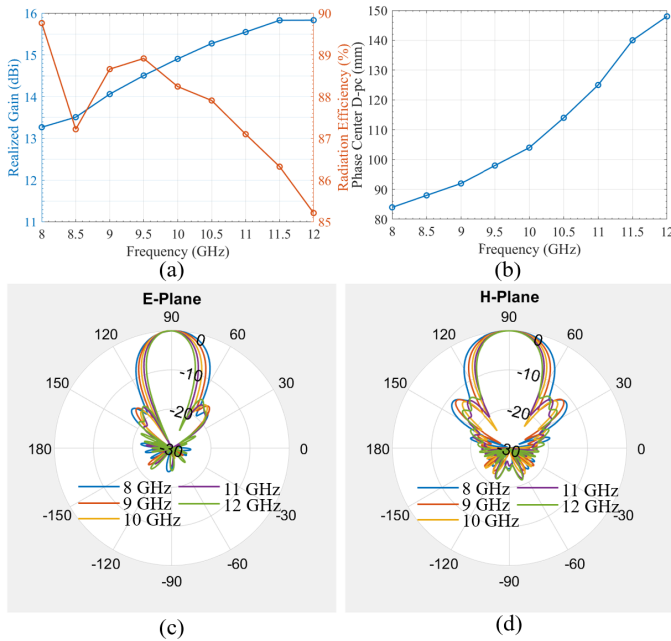


Fig. 11. APFA performance in terms of (a) realized gain and radiation efficiency and (b) phase center response. (c) E-plane normalized radiation pattern. (d) H-plane normalized radiation pattern.

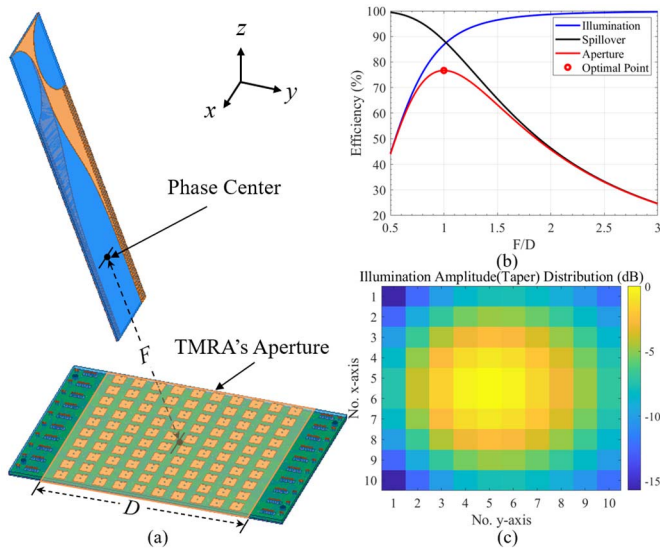


Fig. 12. System configuration. (a) Schematic view of feed. (b) Effect of  $F/D$  on efficiencies of RA antenna system. (c) Normalized taper distribution on 1-bit TMRA aperture when the aperture efficiency is optimal.

The downward trend with increasing frequency of the efficiency is mainly attributed to larger metal and dielectric losses in the high-frequency range. Fig. 11(b) shows the phase center response and demonstrates greater than 65 mm variation in X-band. Besides, the normalized Co-Pol radiation patterns in E-/H-plane are plotted in Fig. 11(c) and (d), indicating the asymmetric radiation characteristic with a wider H-plane and narrower E-plane.

Fig. 12 shows the system design and configuration. To reduce the feed blockage, the APFA is located offset from the normal TMRA aperture with an oblique angle of  $-20^\circ$

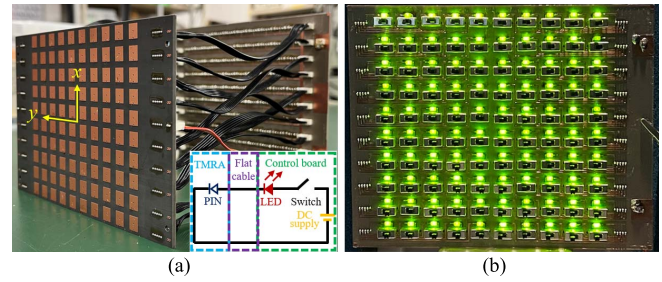


Fig. 13. Control board of 1-bit RA state. (a) Control circuit design. (b) Control board with LEDs all ON.

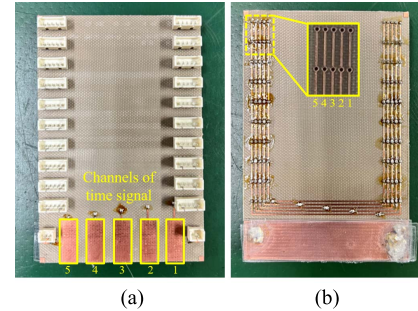


Fig. 14. Control board of TM state. (a) Top view. (b) Bottom view.

in the  $yz$  plane, as shown in Fig. 12(a).  $F$  is the distance between the phase center of APFA and the center of TMRA aperture whose side length is  $D$ . Moreover, for realizing the optimal system performance, which is aperture efficiency, the feed location (described by  $F/D$ ) must be carefully chosen to balance the spillover efficiency and the illumination efficiency [33]. The  $\cos^q$  feed power pattern method is used to calculate the efficiencies mentioned above, and the results are shown in Fig. 12(b), indicating the theoretical maximum aperture efficiency of 76.7% with the  $F/D$  equal 1. Based on the optimal configuration, the final feed position is  $P(0, 34, 96)$  mm and the corresponding taper distribution on the 1-bit TMRA aperture is shown in Fig. 12(c). It should be noted that the edge taper at some positions is larger than the common threshold of  $-10$  dB in RA design [31], which may increase the SLLs of the radiation pattern, especially for large-angle beam scanning. The effect of feed blockage on radiation performance would, however, be more severe when decreasing the  $F/D$  to obtain a lower edge taper due to the small size of the fabricated prototype.

#### D. Control Board

As shown in Figs. 13 and 14, the control boards were designed and fabricated for beam scanning and TM, respectively. Fig. 13 shows the control board that implements the 1-bit RA state (to realize beam scanning). The control circuit design is shown in Fig. 13(a). It can be clearly seen that each bias line is connected in series with a light-emitting diode (LED) indicating the p-i-n diode's state and a slide switch controlling the p-i-n diode's state. The LED matrix also directly displays the 1-bit phase distribution of the TMRA, making the debugging and testing procedure easier and more straightforward. Fig. 13(b) shows a photograph of all lit LEDs on the control board.

The control board that implements the TM state is shown in Fig. 14. Constrained by the quantity of the function generator, each column consisting of ten elements of the 1-bit TMRA prototype is set up as a group for control. As can be seen from the arithmetic example demonstrated in the second part of Section II, the Chebyshev distribution is symmetric about the center of the TMRA. This allows ten groups (100 elements) to be controlled using five-channel time signals (20 elements per channel). The time signal is a square wave signal generated by a function generator, whose high level corresponds to the ON state of the p-i-n diode and the “1” state of the time function, and vice versa. The modulation frequency  $f_{p,i}$  and switch-on duration  $\tau_i$  of the time function are controlled by setting the frequency and duty cycle of the square wave in the function generator, respectively. It can be clearly seen from (8) that the time-modulated equivalent amplitude weighting of the center frequency is independent of the normalized turn-on time  $\tau_{on,i}$ , and thus, the time signal  $\tau_{on,i}$  is set the same for each channel and has  $\tau_{on,i} = 0$ . Note that the control board of TM controls each column of elements, which requires the same amplitude of elements within a column in order to guarantee an effective control effect. In the near-field feed, the amplitude of the elements composing each column varies. Therefore, in the experiment to validate the TM characteristic, the feed should be placed in the far-field region of the TMRA.

It should be pointed out that whether the control boards are designed separately or different feed distances are used for different validation experiments, they are only measures limited by the existing experimental environment and not drawbacks of the proposed concept of 1-bit TMRA.

#### IV. EXPERIMENTAL VALIDATION AND RESULTS

##### A. Reflection Characteristics of $10 \times 10$ 1-bit TMRA

The first experiment is designed to verify the reflection characteristics of the designed TMRA. The results of this experiment will form the basis of the subsequent experiments, as shown in Fig. 15(a). This experiment uses the space-wave method and is performed in the microwave anechoic chamber. A linear polarized standard gain horn antenna of model Flann-16240 is used as the transmitting (Tx) antenna with a gain of 20 dBi. The Tx antenna is connected to the VNA through a coaxial line as the feed source for the experiment. The model of the VNA is Anritsu MS46122B-020, which covers a frequency band from 1 MHz to 20 GHz. The Tx antenna is placed facing the TMRA, and the aperture centers of the Tx antenna and TMRA are coaxial and 1.822 m apart. Both Tx and 1-bit TMRA are vertically polarized. To reduce the influences from the socket area’s ground of the 1-bit TMRA prototype and experimental environment (e.g., control board and supporting structure), the surroundings of the TMRA aperture are shielded with absorbing material. Note that the time domain gating function of the VNA is used in the measurement to eliminate undesired scattering from the experimental environment.

The reflection characteristics of the 1-bit TMRA are obtained by measuring the reflection coefficients of TMRA with all diodes set to ON and all diodes set to OFF, respectively. In addition, the reflected amplitudes for the two states are both normalized to the reflected amplitude of a metal sheet of the same size as the 1-bit TMRA prototype. The measured results are shown in Fig. 15(b). It can be found that the reflected

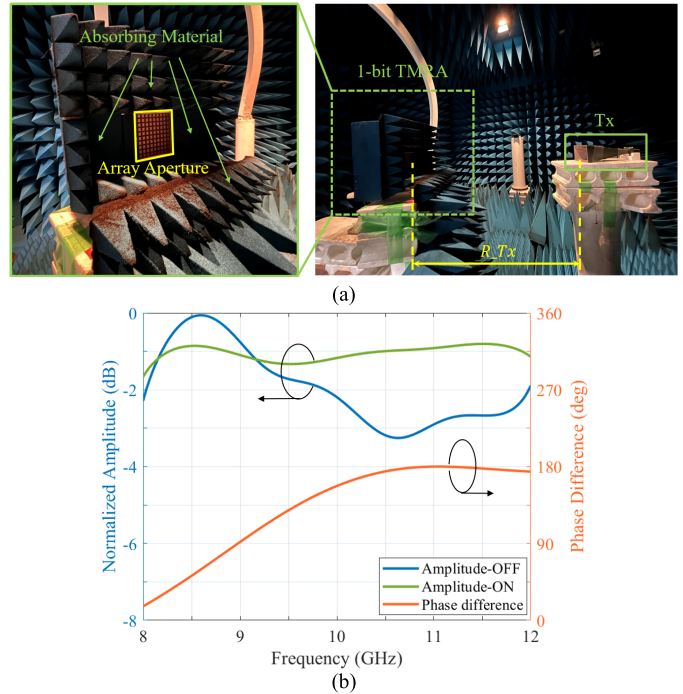


Fig. 15. Measurement of reflection characteristic of 1-bit  $10 \times 10$  TMRA prototype. (a) Experimental environment. (b) Experimental results.

amplitude of the ON state is very stable with a magnitude of  $-4$  dB, while the reflected amplitude of the OFF state has a larger vibration; however, the maximum difference between the reflection amplitudes of the two states is less than 2.2 dB, indicating that the 1-bit TMRA prototype can realize two relatively stable reflection states. From 10.08 to 12 GHz, the phase difference stays within  $180^\circ \pm 20^\circ$ . Specifically, it can be observed from 10.5 to 11.5 GHz that the phase difference is close to  $180^\circ$ , and its curve varies very smoothly. Note that the frequency point of a  $180^\circ$  phase difference between the two states is 11.1 GHz, which is the experimentally verified 1-bit frequency point of the proposed TMRA and operating frequency in the following experiments. Moreover, the amplitude difference is 1.9 dB for the two states at 11.1 GHz.

It should be pointed out that the discrepancies in reflection characteristics of the element are mainly due to the reflection from the ground of the socket area of the fabricated TMRA prototype [shown in Fig. 9(a) and (b)]. The reflection severely interferes with the original reflected fields produced by the TMRA aperture only, thus affecting the reflection characteristics of the 1-bit TMRA prototype. Note that this is a design fault of the control circuit of the fabricated prototype, not a drawback of the proposed 1-bit TMRA concept, and this problem can be completely solved by removing the ground beneath the socket area. Moreover, other common reasons, such as estimated error of the equivalent capacitance in the p-i-n diode modeling [9], inconsistency in the hand soldering of the diodes, and array fabrication error, would also introduce experimental errors.

##### B. Validation of 1-bit Characteristic

As shown in Fig. 16, the measurement system consists of the TMRA system, the rotary table, and the receiving antenna (Rx). The TMRA system includes the TMRA, the

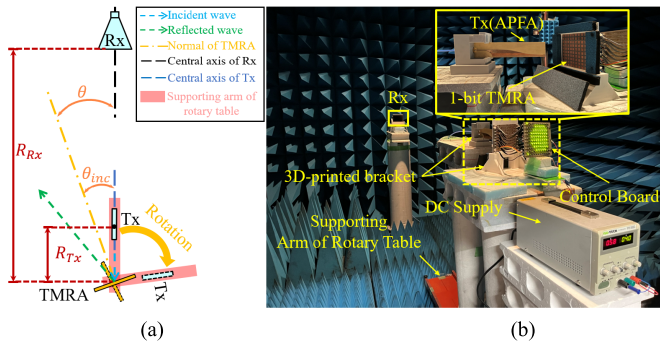


Fig. 16. Experimental environment for validation of beam scanning characteristic. (a) Schema of the measurement system (top view). (b) Overall perspective photograph.

control board, and the feed antenna (Tx). The control board is placed at the back of the TMRA and connected to the TMRA using the flat cables (not marked in Fig. 16). The Tx is vertically polarized, and its location is described by the feed distance  $R_{Tx}$  and feed angle  $\theta_{inc}$ , whose values are determined in the “Feed Source Selection and System Design” part of Section III. The TMRA and Tx are placed at the center and the supporting arm of the rotary table, respectively. The TMRA is fixed by 3D-printed brackets. The surrounding of the TMRA aperture is covered by the absorbing material to decrease the interference of the ground of the socket area. The relative position of the TMRA and Tx is kept constant in the rotation of the rotary table. The Rx is the same horn antenna used in the previous experiment and is fixed in the far-field region of the TMRA with a distance of  $R_{Rx}$ , and the angle between its central axis and the normal of the TMRA aperture is defined as the scanning angle  $\theta$ . Therefore, by rotating the rotary table in the horizontal plane, the radiation pattern of the TMRA can be measured. A photograph of the experimental environment is provided in Fig. 16(b). The relevant parameters are as follows:  $R_{Tx} = 100$  mm,  $\theta_{inc} = -20^\circ$ , and  $R_{Rx} = 2400$  mm. Note that the measured gain of Tx (APFA) at 11.1 GHz is 14.4 dBi.

The 1-bit characteristic is verified by realizing beam scanning using a reconfigurable 1-bit phase distribution. Fig. 17(a) shows the 1-bit phase distribution for different scan angles. The yellow area corresponds to the state “1,” which corresponds to the diode ON state, and the blue area corresponds to the state “-1,” which corresponds to the diode OFF state. The measured radiation patterns of co-polarization (Co-Pol) are plotted in Fig. 17(b). It is observed that the reflected beam of the 1-bit TMRA can be controlled to scan in the range of  $10^\circ - 50^\circ$  with the above phase setting. Note that the slight distortions on the main beams of small scanning directions can be observed, which are mainly caused by the blockage of Tx and feed cable. The radiation performances in terms of gain and maximum SLL for scanned directions are summarized in Table I. In addition, the beam error is  $-3^\circ$  when the scanning beam toward  $50^\circ$ . As aforementioned, the incident angle is  $-20^\circ$ , and therefore, the maximum reflected beam occurs in the  $20^\circ$  direction. The measured gain in this direction is 15.6 dBi, corresponding to a maximum aperture efficiency of 21.1% using the following definition:

$$\eta = \frac{G}{4\pi A/\lambda^2} \quad (12)$$

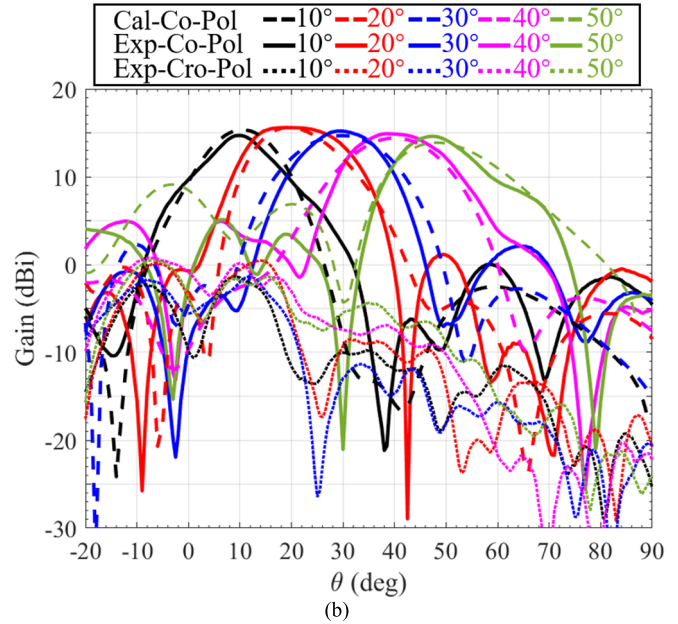
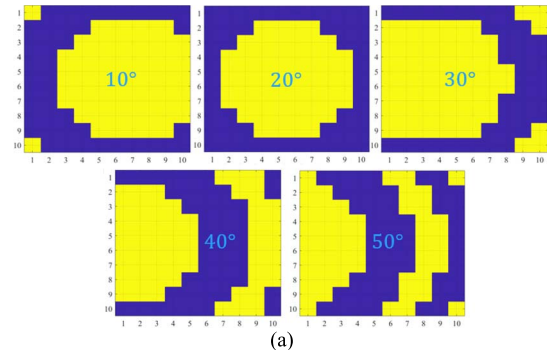


Fig. 17. Experimental result of beam scanning. (a) 1-bit phase distribution for scanning directions. (b) Measured and theoretical radiation pattern.

TABLE I  
MEASURED GAIN AND MAXIMUM SLL AT SCANNED DIRECTIONS

Radiation Performance	$10^\circ$	$20^\circ$	$30^\circ$	$40^\circ$	$50^\circ$
Gain (dBi)	14.7	15.6	15.2	14.9	14.6
Maximum SLL (dB)	-14.7	-14.3	-13.2	-9.7	-9.4

where  $G$  is the measured gain, and  $A$  is the aperture area. Besides, it is observed that the gain variation does not exceed 1 dB within the scanning direction range, indicating the stable radiation performance of beam scanning. In terms of SLLs, good results with the maximum SLL below  $-13$  dB can be observed for the beam scanning range of  $10-30$ . It can also be found that the SLLs become worse for large-angle scanning. This is mainly due to the small aperture size of the fabricated prototype and the large edge taper it causes, which was discussed in detail earlier. Table II lists the loss budget for the main reflection direction ( $20^\circ$ ) at 11.1 GHz. It suggests that the 1-bit phase quantization error is the main reason for the gain loss in this design. The theoretical radiation patterns of Co-Pol calculated by the MATLAB program are also plotted as references. Good agreement can be observed from measured and theoretical results, validating the correctness of

TABLE II  
LOSS BUDGET FOR THE MAIN REFLECTION DIRECTION AT 11.1 GHz

Factor	Loss (dB)
Spillover	0.54
Illumination	0.62
Feed antenna	0.61
1-bit phase quantization	2.56
Diode	0.72
Feed blockage, phase error, metal loss, dielectric loss, others	1.71
Total	6.76

the measurement. Note that the slight differences in the gain variation for the calculation and measurement results may be attributed to the simplified modeling of the ground of socket area in the program and experimental errors. In addition, the cross-polarization (Cro-Pol) is also measured and plotted in Fig. 17(b). The overall relatively high Cro-Pol is mainly caused by the offset feed system [23] and is constrained by the Cro-Pol level of the APFA itself. Although, the results show good polarization purity for all scanning directions, corresponding to the Cro-Pol level (normalized to Co-Pol level) of  $-16.1$ ,  $-22.3$ ,  $-28$ ,  $-22.1$ , and  $-21.2$  dB, respectively.

It should be noted that the gain and SLLs are mainly limited by the large edge taper, which is caused by the small aperture size of the fabricated prototype. Therefore, the gain and SLLs can be improved by increasing the aperture size and configuring a more appropriate feed system. In addition, the specular reflection from the ground of the socket area also increases the SLLs for large-angle scanning. In terms of the aperture efficiency, although it can be slightly improved by increasing the aperture size, i.e., reducing the feed blockage in this work, it is difficult to further improve the aperture efficiency due to the 1-bit phase quantization loss and losses of diodes, which are inevitable in 1-bit RA design. In summary, the 1-bit characteristic of the proposed 1-bit TMRA is verified by the experiment.

### C. Validation of Time Modulation Characteristic

Fig. 18 shows the experimental environment and measurement system to verify the TM characteristic. As aforementioned, Tx should be placed in the far-field region of the TMRA in this experiment. Constrained by the length of the rotary table supporting arm, Tx has finally placed 820 mm away from the center of the TMRA aperture, which almost satisfies the far-field condition. To increase the signal-to-noise ratio in measurement, the horn antenna is adopted as the Tx. The rest of the experimental setup is the same as the previous experiment. Note that the normalized scattering patterns are measured in this experiment to properly evaluate the scattering performance of the proposed 1-bit TMRA. Specifically, all measured results are normalized to the scattering pattern of a metal plate of the same size as the fabricated 1-bit TMRA prototype.

The experimental target is to realize the scattering pattern with  $-20$  dB equal SLLs by means of the TM. The modulation frequency is 100 kHz for all channels. Fig. 19(a) shows the required time sequence of each channel. The dark area

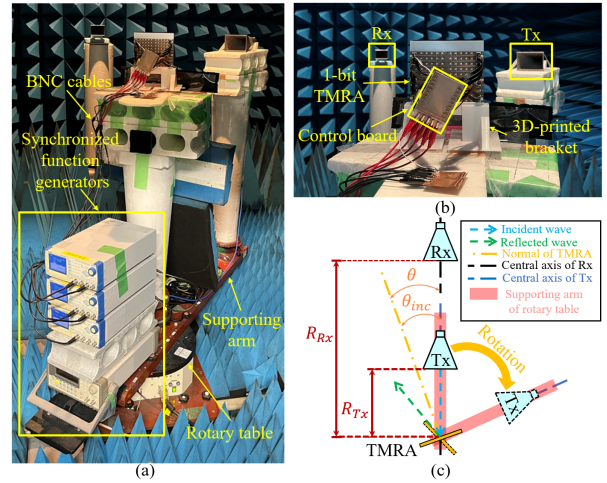


Fig. 18. Experimental environment for validation of TM characteristics. (a) Overall perspective photograph. (b) Detailed photograph of TMRA placement. (c) Schema of the measurement system.

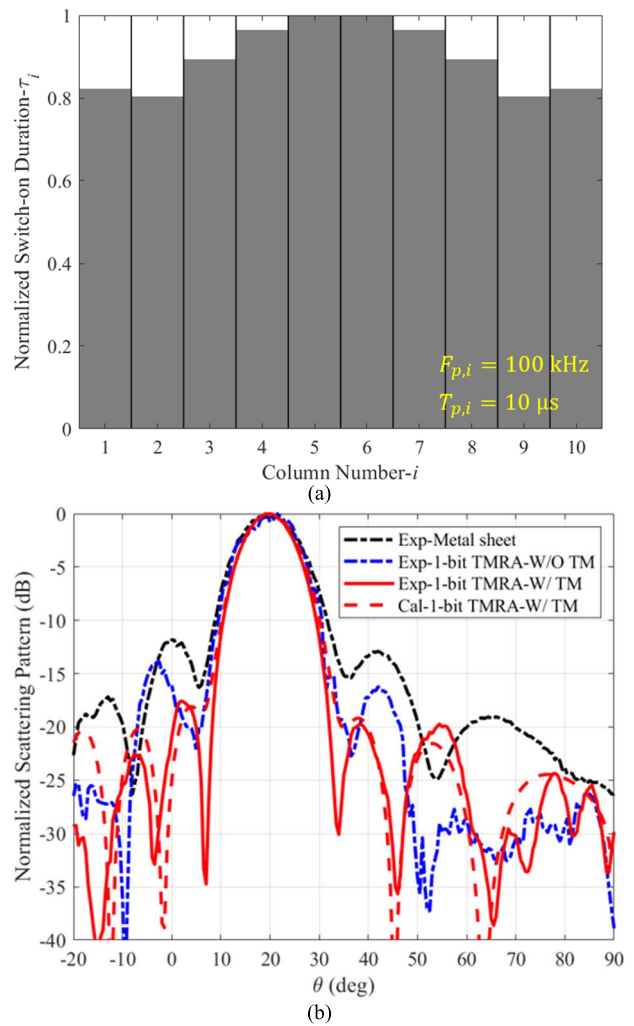


Fig. 19. Experimental results. (a) Switch-on duration  $\tau_i$ . (b) Measured normalized scattering patterns.

corresponds to the state “1,” which corresponds to the diode ON state, and the light square corresponds to the state “ $-1$ ,” which corresponds to the diode OFF state. The measured

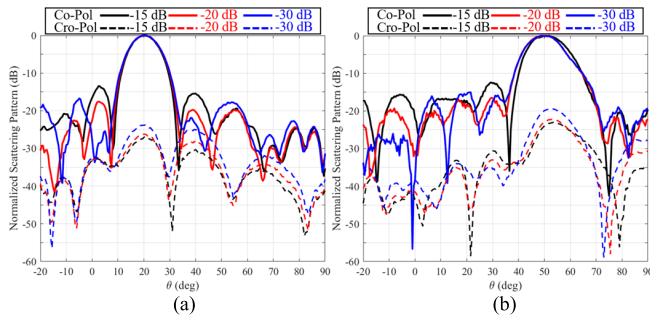


Fig. 20. Measured scattering pattern of different SLLs. (a)  $-20^\circ$  incidence. (b)  $-45^\circ$  incidence.

results are shown in Fig. 19(b). Note that the theoretical calculation result of adopting TM is also plotted as a reference. In addition, the results of the metal sheet are plotted as a benchmark. It is found that the SLLs are significantly reduced by TM. Specifically, except for the first SLL ( $2^\circ$  direction) on the left side of the main beam, the other three SLLs near the main beam are  $-22.53$  dB ( $-7.5^\circ$  direction),  $-19.74$  dB ( $38.5^\circ$  direction), and  $-19.74$  dB ( $54.5^\circ$  direction) respectively. Note that the first SLL is slightly larger than other SLLs. This is caused by the finite distance between the Tx and TMRA, and this phenomenon can be observed in the theoretical result. That is, the experimental target is achieved. In addition, it can be observed that the measured results agree well with the theoretical results, which verifies the correctness of the measurement results. Note that the drop of the received power in the range of  $[-20^\circ, -10^\circ]$  is mainly caused by the Tx antenna's blocking of the reflected wave during the measurement. The other imperfection observed in measured results of using TM is mainly attributed to the existence of the socket area's ground of the fabricated prototype, whose scattering field interferes with the original scattering field produced by the TMRA aperture only. It is worth mentioning that the maximum scattering strength of the result of time modulation is only 1.9 dB, smaller than the results of the metal sheet, which indicates good efficiency of the 1-bit TM. The losses are mainly caused by the appearance of harmonic components and losses of the diodes. In summary, the TM characteristic of the proposed 1-bit TMRA is successfully verified by the experiment.

To further evaluate the performance of the TM, the normalized scattering patterns for both Co-Pol and Cro-Pol of realizing equal SLLs of  $-15$  and  $-30$  dB are measured and plotted together with the results of form equal  $-20$  dB SLLs in Fig. 20. Note that the measured results of  $45^\circ$  incidence are also measured to verify the capability of TM at other incident angles. As can be seen in Fig. 20(a), the measured main beams are the same for the different time sequences, while the sidelobes are different, which indicates that the TM achieves effective control of the SLLs. Specifically, the equal  $-15$  and  $-20$  dB SLLs are clearly successfully achieved. The results of forming  $-30$  dB SLLs show that only the reduction of the first SLL is achieved, while the other SLLs are not effectively controlled. This is also caused by the interference of the ground of the socket area discussed previously. Note that the interference will be more severe when trying to achieve lower SLLs. This is because achieving lower SLLs requires smaller induced currents at the edges of the TMRA's

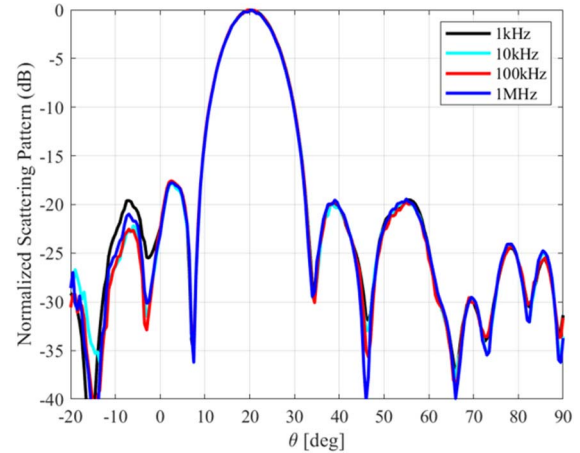


Fig. 21. Measured scattering pattern of different modulation frequencies.

aperture, while the induced currents generated by the ground of the socket area on either side of the aperture are very large. Although the absorbing material is used in experiments to decrease the induced current by the ground, when the required induced current at the edges of TMRA aperture is smaller than the induced current from the ground, the latter will have a decisive role in the generation of SLLs. This is the reason why  $-15$  and  $-20$  dB SLLs can be observed, while  $-30$  dB and lower SLLs cannot be observed by this fabricated prototype. In terms of the SLLs control, the results in Fig. 20(a) and (b) are basically the same, demonstrating that the effect of TM is not affected by the incident angle. Furthermore, high polarization purity can be observed from all measured Cro-Pol results.

The variation of the 1-bit TMRA radiation characteristics with frequency when using the TM is discussed below. The maximum scattering strength of the main beam does not fluctuate more than 1 dB over the entire measurement band (10.75–11.2 GHz). Note that we define an SLL bandwidth as the frequency range in which the difference between the first right SLL and the design target ( $-20$  dB in this experiment) does not exceed 1 dB. The experimental results show that the SLL bandwidth exceeds 250 MHz. From the signal transmission point of view, it is, however, necessary for the bandwidth of the time-modulated signal to be smaller than the TM frequency  $f_p$  (100 kHz in this work) to avoid spectrum aliasing [34]. That is, the operating bandwidth of the proposed 1-bit TMRA system is mainly limited by the TM frequency.

Therefore, the normalized scattering patterns for different TM frequencies are also measured and are plotted in Fig. 21. From 1 kHz to 1 MHz, the measured results remain essentially the same, which verifies that the modulation frequency does not affect the scattering characteristic of the TMRA under the TM state. Note that in this experiment, the upper limit of the modulation frequency is determined by the function generator. This is because when the modulation frequency exceeds 1 MHz, the duty cycle of the square wave signal generated by the function generator does not satisfy the time sequence requirement of forming  $-20$  dB SLLs. In most cases, the modulation frequency is determined by the operating frequency of the switching components (e.g., diodes and MEMS, etc.) and the operating frequency of the time signal

generated by the control board. Note that the TM frequency of TMRA applied to communication can only reach a few megahertz [20] at this stage, which is suitable for narrowband communication. With the development of semiconductor technology, TMRA with larger signal bandwidth will, however, meet the requirements of more communication scenarios.

Although the 1-bit TMRA prototype is fabricated and validated in X-band in this work, the effectiveness of TM technology is independent of the carrier frequency (as long as much larger than the TM frequency). Therefore, the proposed 1-bit TMRA concept can be implemented in any frequency band of interest, such as sub-6G, millimeter-wave, or terahertz band. Also note that although the proposed 1-bit TMRA works in single-linearly polarization, the initial element structure used in this work is possible to be modified to realize dual-linear polarization [35], which is an important requirement for RIS applications in mobile systems. It can be inferred that the complicated bias circuit design would be one of the biggest challenges, and we believe this issue would be addressed in future research to make the proposed 1-bit TMRA more practical.

It is worth pointing out that the interference from the socket area's ground is severe, which deteriorates the overall performance of the fabricated 1-bit TMRA prototype. Although the interference is greatly reduced by covering the absorbing material in the experiment, it cannot be completely eliminated. It is for this reason that leads to the shift of the 1-bit frequency point, increasing the SLLs of beam scanning and limiting the effect of TM. It is, however, not the drawback of the proposed 1-bit TMRA concept, and experiments have fully validated the effects of the proposed concept. In addition, to further improve the performance, we think a well-designed prototype layout, larger aperture size, and more accurate modeling of diodes should be further developed in the future.

## V. CONCLUSION

In this investigation, we successfully designed a 1-bit  $10 \times 10$  TMRA for RIS applications at the X-band and then verified it experimentally. We identified the intrinsic similarities between the reflection states and logic states of the time function and designed the proposed 1-bit TMRA based on our findings. The proposed 1-bit TMRA has the characteristics of the conventional 1-bit RA and can shape radiation patterns through TM at the center operating frequency to cope with different communication scenarios. The main results of this investigation are as follows.

- 1) The proposed 1-bit TMRA successfully realizes beam scanning in the range of  $10^\circ$ – $50^\circ$  by setting the corresponding 1-bit quantization phase to each element, which verifies the 1-bit characteristic. The measured maximum gain is 15.6 dBi with a corresponding aperture efficiency of 21.1% at 11.1 GHz.
- 2) The TM characteristic is verified by shaping the scattering pattern with ultralow SLLs. It is shown that the proposed 1-bit TMRA can achieve a scattering pattern equal to  $-20$  dB SLLs, with a maximum scattering strength of only 1.9 dB less than that of the same size metal sheet. This small reduction of the scattering strength indicates well efficiency of the proposed 1-bit TMRA.

- 3) It is shown that it is not the radiation characteristic bandwidth (i.e., gain and SLL bandwidth) but the TM bandwidth, which is the key factor limiting the bandwidth of 1-bit TMRA operation. The experiment also validated that the modulation frequency does not affect the radiation characteristics of 1-bit TMRA under the TM state.

The findings of this study can be used as a resource for refining the theory of TM technique-based RA design. The proposed 1-bit TMRA has practical potential in RIS applications, and further developments will contribute to beyond 5G and 6G technologies of the future.

## REFERENCES

- [1] T. Otsuji, K. Iwatsuki, H. Yamada, and M. Yashima, "Concept of resilient electric power and information communication technology (R-EICT) converged network systems based on overall optimization of autonomous decentralized cooperative control of DC microgrids," in *Proc. IEEE Power Energy Soc. Innov. Smart Grid Technol. Conf. (ISGT)*, Feb. 2021, pp. 1–5.
- [2] T. Tanaka et al., "Energy-distribution platform technologies toward zero environmental impact," *NTT Tech. Rev.*, vol. 19, no. 6, pp. 22–27, Jun. 2021.
- [3] E. Basar, M. D. Renzo, J. D. Rosny, M. Debbah, M. Alouini, and R. Zhang, "Wireless communications through reconfigurable intelligent surfaces," *IEEE Access*, vol. 7, pp. 116753–116773, 2019.
- [4] M. A. El Mossallamy, H. Zhang, L. Song, K. G. Seddik, Z. Han, and G. Y. Li, "Reconfigurable intelligent surfaces for wireless communications: Principles, challenges, and opportunities," *IEEE Trans. Cogn. Commun. Netw.*, vol. 6, no. 3, pp. 990–1002, Sep. 2020.
- [5] L. Dai et al., "Reconfigurable intelligent surface-based wireless communications: Antenna design, prototyping, and experimental results," *IEEE Access*, vol. 8, pp. 45913–45923, 2020.
- [6] M. A. El Mossallamy, H. Zhang, L. Song, K. G. Seddik, Z. Han, and G. Y. Li, "Reconfigurable intelligent surfaces for wireless communications: Principles, challenges, and opportunities," *IEEE Trans. Cogn. Commun. Netw.*, vol. 6, no. 3, pp. 990–1002, Sep. 2020.
- [7] Z. L. Wang et al., "1 bit electronically reconfigurable folded reflectarray antenna based on p-i-n diodes for wide-angle beam-scanning applications," *IEEE Trans. Antennas Propag.*, vol. 68, no. 9, pp. 6806–6810, Sep. 2020.
- [8] W. Wu, K.-D. Xu, Q. Chen, T. Tanaka, M. Kozai, and H. Minami, "A wideband reflectarray based on single-layer magneto-electric dipole elements with 1-bit switching mode," *IEEE Trans. Antennas Propag.*, vol. 70, no. 12, pp. 12346–12351, Dec. 2022.
- [9] X. Pan, F. Yang, S. Xu, and M. Li, "A 10 240-element reconfigurable reflectarray with fast steerable monopulse patterns," *IEEE Trans. Antennas Propag.*, vol. 69, no. 1, pp. 173–181, Jan. 2021.
- [10] H. Yang et al., "A 1-bit  $10 \times 10$  reconfigurable reflectarray antenna: Design, optimization, and experiment," *IEEE Trans. Antennas Propag.*, vol. 64, no. 6, pp. 2246–2254, Jun. 2016.
- [11] W. H. Kummer, A. T. Villeneuve, T. Fong, and F. Terrio, "Ultra-low sidelobes from time-modulated arrays," *IEEE Trans. Antennas Propag.*, vol. AP-11, no. 6, pp. 633–639, Nov. 1963.
- [12] G. Li, S. Yang, and Z. Nie, "Adaptive beamforming in time modulated antenna arrays based on beamspace data," in *Proc. Asia Pacific Microw. Conf.*, Dec. 2009, pp. 743–746.
- [13] P. Rocca, L. Poli, G. Oliveri, and A. Massa, "Adaptive nulling in time-varying scenarios through time-modulated linear arrays," *IEEE Antennas Wireless Propag. Lett.*, vol. 11, pp. 101–104, 2012.
- [14] E. A. Ball and A. Tennant, "A technique to control the harmonic levels in time-modulated antenna arrays—Theoretical concept and hardware verification platform," *IEEE Trans. Antennas Propag.*, vol. 68, no. 7, pp. 5375–5386, Jul. 2020.
- [15] G. Li, S. Yang, and Z. Nie, "Direction of arrival estimation in time modulated linear arrays with unidirectional phase center motion," *IEEE Trans. Antennas Propag.*, vol. 58, no. 4, pp. 1105–1111, Apr. 2010.
- [16] Y. Tong and A. Tennant, "A two-channel time modulated linear array with adaptive beamforming," *IEEE Trans. Antennas Propag.*, vol. 60, no. 1, pp. 141–147, Jan. 2012.
- [17] Y. Wang and A. Tennant, "Experimental time-modulated reflector array," *IEEE Trans. Antennas Propag.*, vol. 62, no. 12, pp. 6533–6536, Dec. 2014.

- [18] J. Y. Dai et al., "Simultaneous in situ direction finding and field manipulation based on space-time-coding digital metasurface," *IEEE Trans. Antennas Propag.*, vol. 70, no. 6, pp. 4774–4783, Jun. 2022.
- [19] L. Zhang et al., "Space-time-coding digital metasurfaces," *Nat. Commun.*, vol. 9, pp. 1–11, Oct. 2018.
- [20] J. Y. Dai et al., "Realization of multi-modulation schemes for wireless communication by time-domain digital coding metasurface," *IEEE Trans. Antennas Propag.*, vol. 68, no. 3, pp. 1618–1627, May 2020.
- [21] X. Wang and C. Caloz, "Spread-spectrum selective camouflaging based on time-modulated metasurface," *IEEE Trans. Antennas Propag.*, vol. 69, no. 1, pp. 286–295, Jan. 2021.
- [22] J. Wang, D. Feng, Z. Xu, Q. Wu, and W. Hu, "Time-domain digital-coding active frequency selective surface absorber/reflector and its imaging characteristics," *IEEE Trans. Antennas Propag.*, vol. 69, no. 6, pp. 3322–3331, Jun. 2021.
- [23] P. Nayeri, F. Yang, and A. Z. Elsherbeni, *Reflectarray Antennas: Theory Designs and Applications*. Hoboken, NJ, USA: Wiley, 2018.
- [24] C. L. Dolph, "A current distribution for broadside arrays which optimizes the relationship between beam width and side-lobe level," *Proc. IRE*, vol. 34, no. 6, pp. 335–348, Jun. 1946.
- [25] H.-P. Li, G.-M. Wang, T. Cai, J. G. Liang, and X.-J. Gao, "Phase- and amplitude-control metasurfaces for antenna main-lobe and side-lobe manipulations," *IEEE Trans. Antennas Propag.*, vol. 66, no. 10, pp. 5121–5129, Oct. 2018.
- [26] S. V. Hum and J. Perruisseau-Carrier, "Reconfigurable reflectarrays and array lenses for dynamic antenna beam control: A review," *IEEE Trans. Antennas Propag.*, vol. 62, no. 1, pp. 183–198, Jan. 2014.
- [27] X. Cao and Q. Chen, "Design of multifunctional reflectarray elements based on the switchable ground plane," in *Proc. Int. Symp. Antennas Propag. (ISAP)*, Oct. 2021, pp. 1–2.
- [28] P. W. Hannan and M. A. Balfour, "Simulation of a phased-array antenna in waveguide," *IEEE Trans. Antennas Propag.*, vol. AP-13, no. 3, pp. 342–353, May 1965.
- [29] S. V. Hum, M. Okoniewski, and R. J. Davies, "Modeling and design of electronically tunable reflectarrays," *IEEE Trans. Antennas Propag.*, vol. 55, no. 8, pp. 2200–2210, Aug. 2007.
- [30] H. Yang et al., "Design of resistor-loaded reflectarray elements for both amplitude and phase control," *IEEE Antennas Wireless Propag. Lett.*, vol. 16, pp. 1159–1162, 2017.
- [31] H. Zhang, X. Chen, Z. Wang, Y. Ge, and J. Pu, "A 1-bit electronically reconfigurable reflectarray antenna in x band," *IEEE Access*, vol. 7, pp. 66567–66575, 2019.
- [32] H. Sato, Y. Takagi, and K. Sawaya, "High gain antipodal Fermi antenna with low cross polarization," *IEICE Trans. Commun.*, vol. E94-B, no. 8, pp. 2292–2297, 2011.
- [33] J. Huang and J. A. Encinar, *Reflectarray Antennas*. Hoboken, NJ, USA: Wiley-IEEE Press, 2007.
- [34] J. C. Bregains, J. Fondevila-Gomez, G. Franceschetti, and F. Ares, "Signal radiation and power losses of time-modulated arrays," *IEEE Trans. Antennas Propag.*, vol. 56, no. 6, pp. 1799–1804, Jun. 2008.
- [35] H. Yang, F. Yang, S. Xu, M. Li, X. Cao, and J. Gao, "A 1-bit multipolarization reflectarray element for reconfigurable large-aperture antennas," *IEEE Antennas Wireless Propag. Lett.*, vol. 16, pp. 581–584, 2016.



**Xianbo Cao** (Graduate Student Member, IEEE) was born in Xi'an, Shaanxi, China, in 1995. He received the B.S. and M.S. degrees in electromagnetic field and microwave technology from Xidian University, Xi'an, in 2016 and 2019, respectively. He is currently pursuing the Ph.D. degree with the Department of Communications Engineering, Tohoku University, Sendai, Japan.

His current research interests include time-modulated arrays, reflectarray antennas, reconfigurable antennas, metasurface antennas, reconfigurable intelligent surface (RIS), and wireless power transfer (WPT).

Mr. Cao was a recipient of the Best Student Award at the 2018 Asian Wireless Power Transfer Workshop (AWPT 2018) in 2018.



**Qiang Chen** (Senior Member, IEEE) received the B.E. degree from Xidian University, Xi'an, China, in 1986, and the M.E. and D.E. degrees from Tohoku University, Sendai, Japan, in 1991 and 1994, respectively.

He is currently a Chair Professor of the Electromagnetic Engineering Laboratory, Department of Communications Engineering, Faculty of Engineering, Tohoku University. His current research interests include antennas, microwave and millimeter waves, electromagnetic measurement, and computational

electromagnetics.

Dr. Chen is a fellow of IEICE. He received the Best Paper Award and Zenichi Kiyasu Award from the Institute of Electronics, Information, and Communication Engineers (IEICE). He served as the Chair for the IEICE Technical Committee on Photonics-Applied Electromagnetic Measurement from 2012 to 2014, the Chair for the IEICE Technical Committee on Wireless Power Transfer from 2016 to 2018, the Chair for the IEEE Antennas and Propagation Society Tokyo Chapter from 2017 to 2018, and the Chair for the IEICE Technical Committee on Antennas and Propagation from 2019 to 2021.



**Toru Tanaka** received the B.E. and M.E. degrees in quantum science and energy engineering from Tohoku University, Sendai, Japan, in 1996 and 1998, respectively.

He joined the NTT Integrated Information and Energy Systems Laboratories, Tokyo, Japan, in 1998. He was engaged in research on the evaluation of dc power supply system stability and voltage fluctuations. He also developed HVDC power supply systems for telecommunication buildings and data centers. From 2009 to 2012, he was the Manager with NTT FACILITIES, where he developed power supply systems and a smart community. He is currently a Senior Research Engineer and a Supervisor with the NTT Space Environment and Energy Laboratories, Tokyo, Japan, and he is currently researching the energy network.

Mr. Tanaka received the 2003 and 2009 Shibusawa Award from The Japan Electric Association (JEA).



**Masaki Kozai** received the Ph.D. degree from the Tokyo Institute of Technology, Tokyo, Japan, in 2010.

He joined NTT, in 2010. He is currently a Senior Research Engineer with the NTT Space Environment and Energy Laboratories, Tokyo, Japan. His current research interests include energy demand forecast and energy control technologies.



**Hiroya Minami** received the B.E. and M.E. degrees from Seikei University, Tokyo, Japan, in 1994 and 1996, respectively.

He joined NTT, in 1996, where he has been engaged in research on traffic technologies of communications systems, ubiquitous systems, and service delivery platforms. He is currently a Senior Research Engineer with the NTT Space Environment and Energy Laboratories, Tokyo, Japan.

Mr. Minami is a member of IEICE. He received the Young Engineer's Award from the Institute of Electronics, Information, and Communication Engineers (IEICE) in 2003.